Belgian Journal of Zoology
www.belgianjournalzoology.be

ISSN 2295-0451

Research article

https://doi.org/10.26496/bjz.2023.110

Skeletal deformities in gilthead seabream (*Sparus aurata*): exploring the association between mechanical loading and opercular deformation

Vincent Vermeylen [1,2,*], Barbara De Kegel [2], Tania De Wolf [3] & Dominique Adriaens [2]

[1] Laboratory of Aquaculture and Artemia Reference Center, Ghent University, Coupure Links 653, 9000 Gent, Belgium.
[2] Evolutionary Morphology of Vertebrates, Ghent University, K.L. Ledeganckstraat 35, 9000 Gent, Belgium.
[3] INVE, Maricoltura di Rosignano Solvay, srl, Via P. Gigli (Loc Lillatro), 57013 Rosignano Solvay, Italy.

[*] Corresponding author: vincent.vermeylen@ugent.be

Abstract. Fish aquaculture is frequently confronted with skeletal abnormalities. In gilthead seabream (*Sparus aurata* (Linnaeus, 1758)), opercular deformities are one of the most common types of deformities. Many studies point at potential causal factors, mainly genetic or nutritional. However, no clear consensus has surfaced yet, and other factors known to affect bone formation remain unexplored, including mechanical stressors by external forces or muscle contraction. In this study, we investigated whether an altered mechanical use of the gill cover could be associated with opercular deformities, by inducing a change in the respiratory rate and thus gill ventilation. Juvenile seabreams were reared under 80, 100 or 200% dissolved oxygen (DO) to trigger altered respiration behaviour, and the effect on body and opercular shape was analysed. The main hypothesis was that hypoxic conditions would increase opercular ventilation, which would result in a higher prevalence of opercular deformities. The results show that the hypoxic condition (80% DO) did not trigger a significantly higher prevalence of opercular deformations, though the opposite is true for the hyperoxic condition (200% DO). No effect of oxygen treatment was observed on overall body shape, though deformed opercles showed a pronounced, but non-significant difference in shape across treatments. Morphometric results and µCT scans reveal that deformations mainly occur in the dorsocaudal region of the opercular bone. Although no causal link could be demonstrated, we discuss how these results can indirectly suggest that an altered mechanical loading on the operculum could explain its deformation.

Keywords. operculum, deformation, *Sparus aurata*.

Vermeylen V., De Kegel B., De Wolf T. & Adriaens D. (2023). Skeletal deformities cin gilthead seabream (*Sparus aurata*): exploring the association between mechanical loading and opercular deformities. *Belgian Journal of Zoology* 153: 81–104. https://doi.org/10.26496/bjz.2023.110

Introduction

Morphological abnormalities frequently occur in finfish aquaculture, affecting different aspects of the fish's morphology, especially at the skeletal level. This ranges from the overall shape to specific skeletal parts such as the cranium, the vertebral column, or the fins (Divanach *et al.* 1996; Koumoundouros 2010). Deformities in a cultured stock have multiple consequences. Spinal, fin or swimbladder issues affect swimming performance (Chatain 1994) while deviations in the cranial skeleton can influence feeding performance (Koumoundouros *et al.* 1997). Some abnormalities, such as opercular deformities, affect the respiratory efficiency, which leaves the fish more susceptible to hypoxic stress but also to increased exposure to gill parasites (Paperna *et al.* 1980; Beraldo *et al.* 2003). A reduced biological performance, lethal or not, also results in a reduced market value associated with a downgrading of the image of the product (Noble *et al.* 2012). Frequencies of deformities can be substantial, ranging up to 80% of the stock (Divanach *et al.* 1996; Boglione *et al.* 2013), though prevalences have dropped in the last decades, likely due to improved fish husbandry (Koumoundouros 2010; Prestinicola *et al.* 2014). Still, such abnormalities remain a problem in a time when both food quality and appearance strongly influence the customer's confidence in aquaculture products.

Many factors have been identified as possible causes for deformities, ranging from nutritional, genetic and polluting sources to abiotic parameters, including hydrodynamic conditions and stocking density (Roo *et al.* 2010; Boglione *et al.* 2013; Sfakianakis *et al.* 2015; Kuroki *et al.* 2016). However, little attention has been given to the mechanical induction of skeletal deformities, although it is known that the mechanical environment controls bone formation and is even essential for it (Witten & Huysseune 2009). The large number of causative factors makes the investigation of morphological abnormalities a complex problem.

In 2020, gilthead sea bream represented 9% of the total EU aquaculture production in volume, and 13% in real value (EUMOFA 2022). Although sea bream husbandry has greatly improved in the last decades, skeletal anomalies remain a frequently occurring issue, with percentages of affected fish ranging from 2 to 50% (Koumoundouros *et al.* 2010; Georgakopoulo *et al.* 2010; Prestinicola *et al.* 2014; García-Celdrán *et al.* 2016). The most common anomaly is found in the operculum, with a prevalence of 6 to 32% (Verhaegen *et al.* 2007; Ortiz-Delgado *et al.* 2014; García-Celdrán *et al.* 2015). Such deformities involve the opercular and subopercular bone and can be uni- or bilateral (symmetrical and asymmetrical), where unilateral deformations seem to indicate a fluctuating asymmetry (Verhaegen *et al.* 2007). During normal ontogeny, the opercle forms through an appositional deposition of acellular bone, leading to the ossification in the opercular skin fold. This skin fold is detectable at 7 DPH (days post-hatching), and the onset of ossification occurs as a very thin opercle at 14 DPH (Ortiz-Delgado *et al.* 2014; Thuong *et al.* 2017). The first signs of an opercular deformity are detectable around 17–19 DPH, at 4.5 mm total standard length (defined as the length from the tip of the nose to the caudal tip of the notochord in early larval stages or to the tip of the caudal peduncle in later stages) (Galeotti *et al.* 2000; Thuong *et al.* 2017). Opercular deformities are sometimes associated with deformities in the branchiostegal rays and to a lesser extent in the preopercular bone (Koumoundouros *et al.* 1997). When deformed, these structures generally show an inward folding into the gill cavity (Galeotti *et al.* 2000; Beraldo *et al.* 2003; Verhaegen *et al.* 2007).

During early ontogeny, the opercular fold is not yet supported by bone, making it more susceptible to bending due to mechanical forces from water flow. Mechanical stressors affect the ossification and mineral content of the bone matrix, thereby altering the mechanical properties of the bone (Totland *et al.* 2011). In cellular bone, osteocytes are the mechanosensors that can respond to different stimuli, including (changes in) mechanical strain (Bonewald 2011; Witten & Hall 2015). However, Sparidae lack osteocytes embedded in the bone matrix (Ekanayake & Hall 1988). With no osteocytes present, the role of mechanosensing is likely attributed to osteoblasts (Shahar & Dean 2013; Atkins *et al.*

2015), although a recent study suggests that the absence of osteocytes in this bone should be reconsidered (Ofer *et al.* 2019). In *S. aurata*, opercular osteoblasts are mainly localized around the posterior edge of the bone, indicating that matrix deposition is concentrated there (Thuong *et al.* 2017). Deformed opercles also contain thinner collagen fibres (Fernández *et al.* 2011; Thuong *et al.* 2017) and show increased mineralization levels in some parts (Morel *et al.* 2010; Thuong *et al.* 2018), two factors that will alter its material properties and thus how it will respond to mechanical stress. Considering that bone morphogenesis is partially controlled by mechanical stressors (Witten & Huysseune 2009; Ortiz-Delgado *et al.* 2014), an altered mechanical regime acting upon the opercular bone may provide an unexplored explanation for the occurrence of opercular deformities.

Contracting muscles also induce mechanical loading on skeletal structures. For example, abnormal bone deposition on the ossifying pre-haemal vertebrae of sea bass was observed under hyperactivity of the pre-haemal muscles (Kranenbarg *et al.* 2005). Excessive lateral movement of the operculum during gill ventilation could be expected to co-occur with increased mechanical loading, especially at the attachment sites of the antagonistic muscles acting upon it (i.e., an abducting musculus dilatator operculi, and an adducting musculus adductor operculi) (Winterbottom 1973). An increasing oxygen demand or a decreased DO (dissolved oxygen) level in the water would then trigger an increased opercular ventilation effort through a higher ventilation frequency and abduction amplitude (Cerezo & García García 2004). Most aquatic respiratory fish species hyperventilate as a response to hypoxia, although the oxygen level threshold for a hyperventilatory response is very species-specific (Perry *et al.* 2009). Martos-Sitcha *et al.* (2019) and Ferrer *et al.* (2020) observed a close relationship between oxygen consumption and opercular moving frequency in sea bream and sea bass after exposure to different physical activities. In both cases, increased opercular muscle activity then results in an increased mechanical loading at the insertion sites, and an increased load can be expected all over the operculum, as it pushes against the water. We hypothesize that a sustained and increased opercular ventilation alters the loading pattern, which could lead to an opercular malformation. Morel *et al.* (2010) and Thuong *et al.* (2018) observed a denser mineralization in the caudal region of the fold, corroborating our hypothesis that an increased osteogenic response may result from an increased mechanical loading.

The current study tested this hypothesis by triggering an altered opercular ventilation regime through different DO conditions. By changing the mechanical loading pattern that comes with this setup, we wanted to test whether hypoxic or hyperoxic conditions can trigger abnormal opercular phenotypes. We expected to find more opercular deformities under hypoxic than under normoxic and hyperoxic conditions. We also assessed to what degree these treatments affect the overall body phenotype, and to what degree abnormal opercular phenotypes are associated with particular body shapes.

Material and methods

Hatching and rearing conditions

Samples of gilthead sea bream (*Sparus aurata* (Linnaeus, 1758)) were obtained from the commercial sea bream hatchery in Maricoltura di Rosignano Solvay, Italy. All eggs originated from the same set of 60 broodfish and were spawned at a temperature of 17.5°C. After two days in a tank with continuous water renewal, they hatched at a temperature of 18.5°C. At hatching (i.e., 0 DPH), larvae were stocked in three larval rearing tanks of 6000 litres each, with 650 000 larvae per tank. From 7 DPH onwards, each tank was exposed to a different water oxygenation regime: 80%, 100% or 200% dissolved oxygen (DO), with a concentration of 5.6, 6.8 and 14 mg O_2 per litre, respectively. DO levels were measured with OxyGuard oxygen probes and were increased using liquid oxygen. For the hypoxic condition, we selected the lowest acceptable DO level that would not compromise fish survival, i.e., 80% DO (Pavlidis & Mylonas 2011). After 23 DPH, the larvae were transferred to weaning tanks of 10 000

litres each, still under the same oxygen level conditions, at 170 000 larvae per tank. From 3 to 30 DPH, MIC-F (INVE Technologies, Dendermonde, Belgium), a probiotic mixture containing *Bacillus* strains that improve fish larvae health by increasing water quality and suppressing pathogenic bacteria, was added to the rearing water. Temperature and salinity in rearing and weaning tanks were kept close to 17.5°C and 38‰, respectively. The light intensity regime was adjusted from 400 to 800 lux at 4 DPH and to 8 500 lux when transferred to the weaning tanks. The entire rearing system is semi-closed, with 30% of new seawater entering the system daily. Water renewal was set at 150% on 0–3 DPH and increased gradually from 70% at 4 DPH to 300% at 42 DPH. From 3–28 DPH, microalgae (Monzon *Nannochloropsis* followed by INVE Sanolife GWS) were added to create a green-water environment. All fish were raised with the same feeding regime: live feed was provided starting on 3 DPH (rotifers, INVE Artemia AF strain and INVE Artemia EG strain consecutively), supplemented with artificial diets from 24 DPH onwards (INVE Proton ½, INVE Proton ⅔, INVE Proton ¾ and INVE Proton ⅗ consecutively). Mortality was assessed by siphoning and collecting the dead larvae. The initial mortality was estimated on 2 DPH. From 15 DPH onwards, coinciding with the onset of ossification of the opercle, mortality was monitored every 2nd day, and daily from 32 DPH onwards.

Samples

Samples from each oxygen treatment were collected at six points in time, with approximately one week between every sampling point (i.e., at 20, 27, 34, 40, 48, 55 DPH) and sample size varying from 24 to 35 specimens, totalling 540 specimens. Samples were collected from 20 DPH onwards, when the opercular bone is sufficiently developed and actively used for ventilation. At earlier stages, larvae obtain oxygen partially through passive diffusion through the skin. All sampled specimens were anaesthetized and killed by means of an overdose of MS-222, fixed and stored in 4% buffered formalin, and gradually transferred into 30%, 50% and finally 70% ethanol solution. All specimens were stained whole-mounted with a 0.1% Alizarin red solution for 1.5 to 2 hours, depending on the size of the animals. This staining allows a more detailed visualization of the mineralized structures, required for identifying the landmarks and opercular outlines for the shape analyses.

Image acquirement

All specimens were photographed using an Olympus SC30 digital camera mounted on an Olympus SZX9 stereoscopic microscope, with images acquired by analySIS getIT software (ver. 5.1; Olympus Soft Imaging Solutions GmbH; www.olympus-sis.com). Before photographing, the specimens were positioned as horizontal as possible in a petri dish and carefully covered with a microscopic slide (large specimens) or cover slip (smaller specimens) to minimize lateral flexion of the body, without compressing the specimen. Specimens were positioned to ensure that bilateral anatomical structures overlapped as perfectly as possible, to minimize any possible shape variation due to suboptimal positioning. Both the whole body and a close-up of the head region were photographed from both lateral sides (see further), with a scale included in each picture (piece of millimetre sheet). Specimens that could not be photographed due to an extreme flexion of the body (either due to natural causes or through fixation) were omitted from further analysis (12 in total). As opercular deformations can occur unilaterally, all right-side pictures were mirrored so that they could be combined with the left-side data in the morphometric analyses.

Body measurements

On whole body-images, distances between specific morphological points were measured using the FIJI ImageJ software (FIJI, 1.51w; www.imagej.net; Schindelin *et al.* 2012; Schneider *et al.* 2012). The picture was positioned to make sure that the body was set horizontally. Vertical reference lines were then

set at the tip of the snout (i.e., the most rostral point of the head), the frontal edge of the eye, the frontal edge of the cleithrum, the caudal edge of the opercular bone and the caudal edge of the caudal peduncle. On individuals that displayed a mild dorsoventral flexion, we performed a correction by applying the 'segmented line option'. This option allows to draw lines under an angle, at the point of flexion, and measure them as one distance.

The following distances were measured (Fig. 1a): standard length (SL): from the tip of the snout to the caudal edge of the peduncle; snout length (SnL): from the tip of the snout to the frontal edge of the eye; head length (HL): from the tip of the snout to the caudal edge of the cleithrum (unlike many sources in literature, head length was not chosen as the distance up to the caudal opercular edge, because the opercular morphotype would then bias any relationship with the head length); head depth (HD): the height of the head in the postorbital region, just in front of the supraoccipital bone. Finally, the distance between the tip of the snout and the caudal edge of the operculum was measured, and by subtracting this distance from HL, we obtained a quantitative measure for the degree of opercular shortening, further referred to as the gap width (GW). A negative GW refers to an operculum overlapping the cleithrum (normal phenotype), while a positive value refers to an operculum not reaching the cleithrum (deformed phenotype). This last measurement can only be used when individuals display a fully formed gill cover (whether deformed or not). As such, the GW could only be measured for individuals of 48 and 55 DPH. Additionally, SL was assumed not to differ between lateral sides in case of an opercular deformation and the average over both sides was used as a size proxy for the entire specimen.

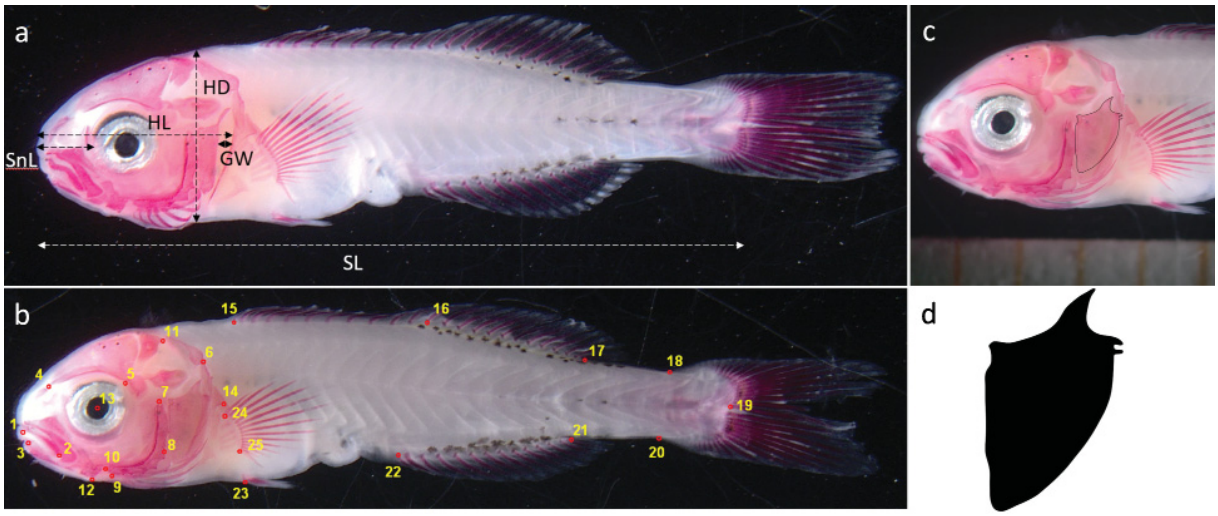

Figure 1 – **a**. 55 DPH old, deformed specimen; standard length (SL), snout length (SnL), head length (HL), head depth (HD) and gap with (GW). **b**. 55 DPH old, normal specimen, with an overview of the landmark locations. **c**. traced outline of an operculum. **d**. Silhouette of the operculum, as used for the outline analysis.

Landmark acquisition and body shape analysis

Homologous landmarks were chosen to capture a reliable representation of the shape variation in the skull and the overall external morphology and were clearly distinguishable on every specimen. Only specimens from 48 and 55 DPH were used for the shape analysis, as these developmental stages allow to identify a sufficient number of homologous landmarks in a reliable manner. The selected landmarks are either type 1 (positions where more than 2 structures meet), 2 (maxima of curvatures and extrusions, such as the tip of a bone or teeth) or 3 ('extremes' or special and rare landmarks, such as the centroid of

TABLE 1

List of landmarks with their description and type. For a definition of each type, see ROHLF & BOOKSTEIN (1990).

Landmark	Description	Type
1	Anteroventral tip of the premaxillary bone	II
2	Caudal tip of the premaxillary bone	II
3	Anterior tip of the dentary bone	II
4	Dorsal tip of the mediodorsal suture between the nasal and frontal bone	I
5	Anterodorsal tip of the sphenotic bone	I
6	Posterior tip of the post-temporal bone	II
7	Posterodorsal tip of the pre-opercular bone	II
8	Overlapping point of the subopercular-interopercular bone suture with the posterior margin of the pre-opercular bone	II
9	Anterior tip of the interopercular bone	II
10	Anterior tip of the pre-opercular bone	II
11	Posterior tip of the parietal bone	II
12	Posteroventral tip of the retro-articulare of the mandibular bone	II
13	Centre of the eye	III
14	Caudal tip of the cleithrum	II
15	Base of the first spine of the dorsal fin	II
16	Base of the first soft ray of the dorsal fin (12^{th} fin ray)	II
17	Base of the last soft ray of the dorsal fin	II
18	Dorsal onset of the caudal fin	I
19	Caudoventral tip of the third hypural bone	II
20	Ventral onset of the caudal fin	I
21	Base of the last fin ray of the anal fin	II
22	Base of the first fin ray of the anal fin	II
23	Bony base of the pelvic fin	II
24	Base of the last (upper) fin ray of the pectoral fin	II
25	Base of the first (lower) fin ray of the pectoral fin	II

a structure). For a more detailed description of each landmark type, see ROHLF & BOOKSTEIN (1990). The landmark dataset was constructed using tpsUtil, while tpsDig was used to digitize the landmark positions on the whole-body images of both lateral sides (ROHLF 2015). Landmarks are based on those from VERHAEGEN *et al.* (2007) and set at the positions as described in Table 1 and shown in Fig. 1b. No landmarks were set on the operculum, as this would bias the comparison of the shape co-variation between overall body and gill cover.

Landmark coordinates were corrected for variation in size, position and orientation with a General Procrustes Analysis (GPA) (ROHLF & SLICE 1990). The variation in the obtained shape coordinates was described by a principal component analysis (PCA). To assess potential erroneous projection from the Kendal (non-Euclidean) shape space onto the Euclidean shape space, the Pearson's product-moment correlation between the shape distances from both shape spaces was calculated, using tpsSmall (ROHLF 2015). The correlation coefficient was maximal ($r = 1.000$, $p < 0.001$), making the dataset suitable for further statistical analyses. SL was used as a size parameter, because it was more easily obtained and

interpretable in a practical context than the normally used centroid size. SL also correlated strongly with centroid size (r=0.996). All analyses on landmark configurations were done using the R package Geomorph ver. 3.1.2 (ADAMS *et al.* 2013, 2018).

To minimise measuring errors in the landmark digitisation (digitisation error and variation in the orientation of the specimen for imaging), an error analysis was performed. Digitisation error refers to the ratio of relative deviation in the digitized landmarks over the deviation between the specimens. This offered an estimate on the magnitude of personal (digitization and orientation) error, compared to the variation between specimens. Digitization error was estimated by digitizing the same picture of a single specimen ten times, assessing the variation of landmark allocation by the researcher. For the orientation error, one specimen was photographed ten times, but every time the specimen was taken out of and repositioned in the petri dish. For both error datasets, the average Procrustes distance over all clusters of replicas was divided by the average Procrustes distance of all the clusters as one dataset. This expressed the amount of digitization and total personal error with respect to the entire shape variation. Orientation error was then obtained by subtracting digitization error from the total personal error. The lower the ratio, the more power can be expected from any analysis conducted with the same method of digitisation and orientation.

Opercular outline acquisition and analysis

Shape variation of the opercular bone was analysed by an outline analysis. Only 55 DPH specimens were used, because they have sufficiently developed opercles that reduce ontogenetic shape variation. The outline of the opercular bone was traced manually on pictures from both lateral sides of the head region, using Inkscape ver. 0.92.3 (www.inkscape.org). The outline was then transformed to a black shape on a white background (Fig. 1c–d), allowing an accurate and automated tracing of the contour. Jpeg-files of these images were processed in the R package Momocs ver. 1.2.9, in which all outline analyses were performed (BONHOMME *et al.* 2014). Shape descriptors were generated with an Elliptic Fourier analysis (EFA) (KUHL & GIARDINA 1982), where shapes were aligned and superimposed. The obtained Fourier coefficients were used for further multivariate analysis (see below).

CT scans

Once stained and photographed, specimens with normal and deformed opercula were selected from the 48 and 55 DPH samples, displaying a range of opercular phenotypic varieties. These specimens were µCT-scanned to obtain a 3D visualization of the opercular morphotypes and the associated bones. Histological studies on opercular deformities indicate that deformed opercular bones often display an inward folding. A 3D view allows to observe and describe more accurately the severity and the region of the deformation and provides insight in the relationship with the opercular ventilation muscles. Scans were performed with the HECTOR µCT-scanner at the Centre for X-ray Tomography (UGCT) at Ghent University. The following settings were used: 70kV tube voltage and 801 projections over 360°. The pixel pitch of the detector was 400 µm, with a reconstructed voxel size of 14.06 µm. Projections were processed and reconstructed using the CT software Octopus (VLASSENBROECK *et al.* 2007). CT data was 3D rendered with Amira 5.5.0 (Visage Imaging, San Diego, CA, USA), using the voxel rendering tool, wherein the bones of interest were segmented, and their surfaces rendered for a complete 3D overview.

Statistical analyses

Statistical analyses were conducted in the statistical package R ver. 3.5.0 (R Core Team 2018). Differences in prevalence between treatments were analysed with Fisher Exact Tests. Data on body measurements were subjected to PCAs and a MANOVA test for each age group, with the measured variables as dependent factors, and treatment and opercular morphotype (based on the GW value) as categorical, independent variables. A log linear model was fitted to compare the growth curves between

the different treatments. All PCAs were assessed with a broken-stick model that identifies the relevant principal components (MacArthur 1957). Test results are considered significant when $p < 0.05$.

For the landmark data, the relationship between the factors 'treatment' and 'opercular morphotype' was tested with a general linear model. With a Procrustes linear model, we assessed the relative amount of overall body shape variation by the independent variables 'treatment' and 'opercular morphotype', while taking standard length into account. Pairwise tests were then performed between treatment groups, using the procD.lm function. PCA plots were made with the plotTangentSpace function.

Outline data were analysed using the Momocs package. The number of relevant harmonics (with each harmonic described by four Fourier coefficients) was selected based on the percentage of shape variation they explain. The first harmonics that cumulatively cover 99% of the shape variation were retained for subsequent analyses. Outline shape data (Elliptic Fourier coefficients) were then submitted to a PCA. The scores of the relevant PCs (selected via a broken-stick model) were subjected to a MANOVA test, with categorical variables opercular morphotype and treatment as independent factors. Mean shapes between treatments and opercular morphotypes were then compared.

Results

Survival and prevalence of deformities

At 2 DPH, prior to exposure to the different DO treatments, the initial mortality was estimated at 19.7, 21.5 and 17.8 % for the three rearing tanks. Up to 32 DPH all treatments displayed a similar trend in mortality. During the subsequent five days, mortality slightly increased more in the 200% DO treatment. By 55DPH, mortality had increased with 0.4, 0.6 and 0.8% for the 80% DO, 100% DO and 200% DO treatment, respectively.

Fully developed opercula could already be recognized at 40 DPH, but in less than 50% of the specimens. Of those with a completely developed operculum, only a minor fraction (< 5%) showed deformed opercula. Only specimens of 48 and 55 DPH were further considered, yielding a sample size of 191 specimens with completely developed opercula. 27.2% of these had a positive GW value, and thus displayed an opercular malformation. In 15, the deformation was bilateral (Table 2).

TABLE 2

Prevalence of normal vs deformed opercular morphotypes, for each age and treatment group. Values between brackets represent the percentage of specimens with a deformation for the treatment at that age. The relative GW is presented as the GW/HL ratio, includes deformed opercles only, and is reported as average ± standard deviation.

Age	**48 DPH**			**55 DPH**			
Treatment	**80% DO**	**100% DO**	**200% DO**	**80% DO**	**100% DO**	**200% DO**	**Total**
Normal	24	22	14	30	27	22	139
Deformed	9 (27.3)	7 (24.1)	14 (50)	5 (14.3)	7 (20.6)	10 (30.3)	52 (27.2)
Unilateral left	3	2	5	4	1	4	19
Unilateral right	3	4	3	1	3	4	18
Bilateral	3	1	6	0	3	2	15
Average relative GW	0.024 ± 0.018	0.036 ± 0.031	0.031 ± 0.012	0.055 ± 0.030	0.056 ± 0.033	0.049 ± 0.022	

A Two-sided Fisher Exact Test revealed a significant difference in the prevalence of deformed opercula between the oxygen treatments ($p=0.03281$). Similar results were obtained when testing both ages (48 and 55 DPH) separately (Cochran-Mantel-Haenszel chi²-test, $p=0.02503$). Deformations showed an increased prevalence at 200% DO (Table 2). No significant difference was found in left versus right prevalence ($p=1$), indicating no association between the presence of a deformation and the side it appeared on.

Body measurements

Body measurements of all 528 specimens were analysed. The variables SL, SnL, HL and HD correlated strongly (Pearson correlation coefficients between 0.967 and 0.994). For none of these variables a difference was found between the treatments in the 48 and 55 DPH samples (Table 3). At younger ages, only very minor differences were observed. A log linear model fitted to the growth curve (SL vs DPH) showed no treatment effect ($p=0.7645$) on growth (Fig. 2). SL changed according to $SL=3.42 \times e^{0.04d}$ ($R^2_{adj}=0.89$, with d the age in DPH).

A PCA with broken-stick analyses of all body measurements, except GW, showed that only the first principal component was relevant, explaining 98.6% of the variation. Factor loadings on PC1 confirmed it being an overall size factor (Fig. 3). PC2 represented 1.1% of the variation and was mainly negatively correlated with SnL. In the plot of PC1 vs PC2, specimens in the upper left quadrant were smaller and had relatively short snouts, while those in the lower right quadrant were larger, and had relatively large snouts. No clustering associated with treatment was observed, indicating that different DO treatments did not consistently affect the body parameters measured here.

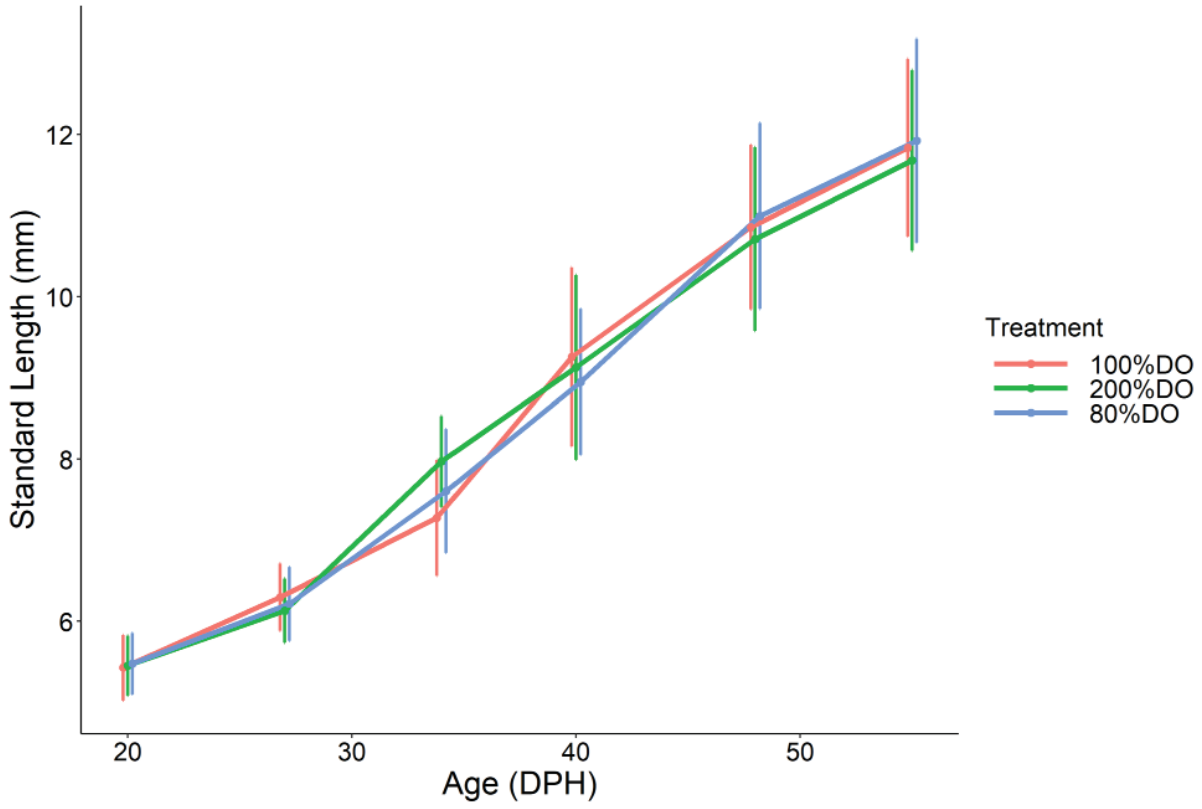

Figure 2 – Growth curves for each treatment. Error flags represent standard deviation.

TABLE 3

Overview of the body measurements per treatment (left columns) and opercular morphotype (right columns), for 48 and 55 DPH. Reported as average ± standard deviation, in mm unit size. Significance codes: *** = < 0.001; ** = < 0.01; * = < 0.05; . = < 0.1.

48 DPH	80% DO	100% DO	200% DO	Sign.	Normal	Deformed	Sign.
SL	11.00 ± 1.15	10.86 ± 1.01	10.71 ± 1.13		11.10 ± 0.95	10.03 ± 1.20	***
SnL	0.82 ± 0.11	0.79 ± 0.11	0.78 ± 0.10	.	0.82 ± 0.10	0.71 ± 0.10	***
HL	2.79 ± 0.30	2.74 ± 0.27	2.73 ± 0.28		2.81 ± 0.25	2.57 ± 0.31	***
HD	2.32 ± 0.29	2.31 ± 0.24	2.26 ± 0.26		2.35 ± 0.23	2.11 ± 0.29	***
55 DPH	80% DO	100% DO	200% DO		Normal	Deformed	
SL	11.92 ± 1.25	11.84 ± 1.09	11.68 ± 1.11		11.90 ± 1.14	11.29 ± 1.15	*
SnL	0.92 ± 0.14	0.89 ± 0.12	0.90 ± 0.13		0.91 ± 0.12	0.86 ± 0.16	.
HL	3.16 ± 0.39	3.13 ± 0.31	3.10 ± 0.34		3.15 ± 0.35	3.04 ± 0.35	
HD	2.64 ± 0.35	2.62 ± 0.28	2.59 ± 0.31		2.63 ± 0.31	2.54 ± 0.34	

When including GW, the normal versus deformed opercular morphotypes could be compared (for 48 DPH and 55 DPH). Normal specimens had a significantly larger SL at both ages (Table 3). SnL, HD and HL were only significantly different at 48 DPH. The frequency distribution of GW over all treatments revealed a bimodal distribution, reflecting both opercular morphotypes (Fig. 4a). Subtle differences were found between treatments, displaying bi- or trimodality, with slightly more variation in the deformed group (Fig. 4b). No pronounced differences were observed between lateral sides. A PCA and broken-stick on the data from 48 and 55 DPH, now including GW, showed the first PC to be relevant, explaining 79.2% of the variation. PC1 was a size factor (Fig. 5), with an increase in overall size associated with a small decrease in GW (reflecting the larger size in normal specimens). There could be a bias from the more numerous normal opercular morphotypes in the dataset, leading to, on average, larger individuals

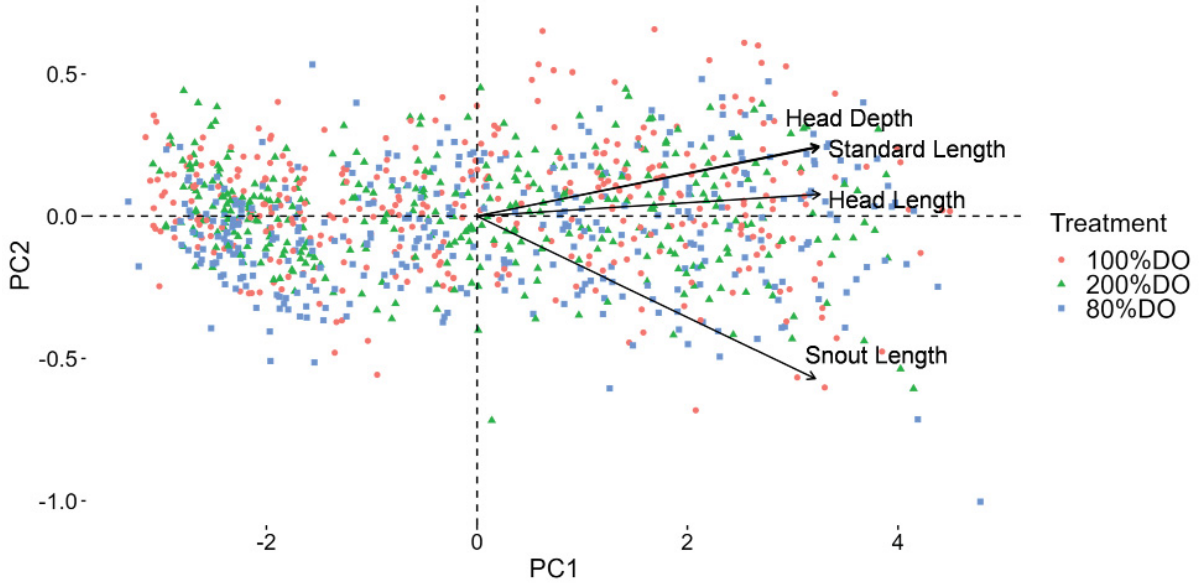

Figure 3 – PCA biplot of all body measurements (gap width not included) on specimens of 48 and 55 DPH. Colour coding is according to treatment.

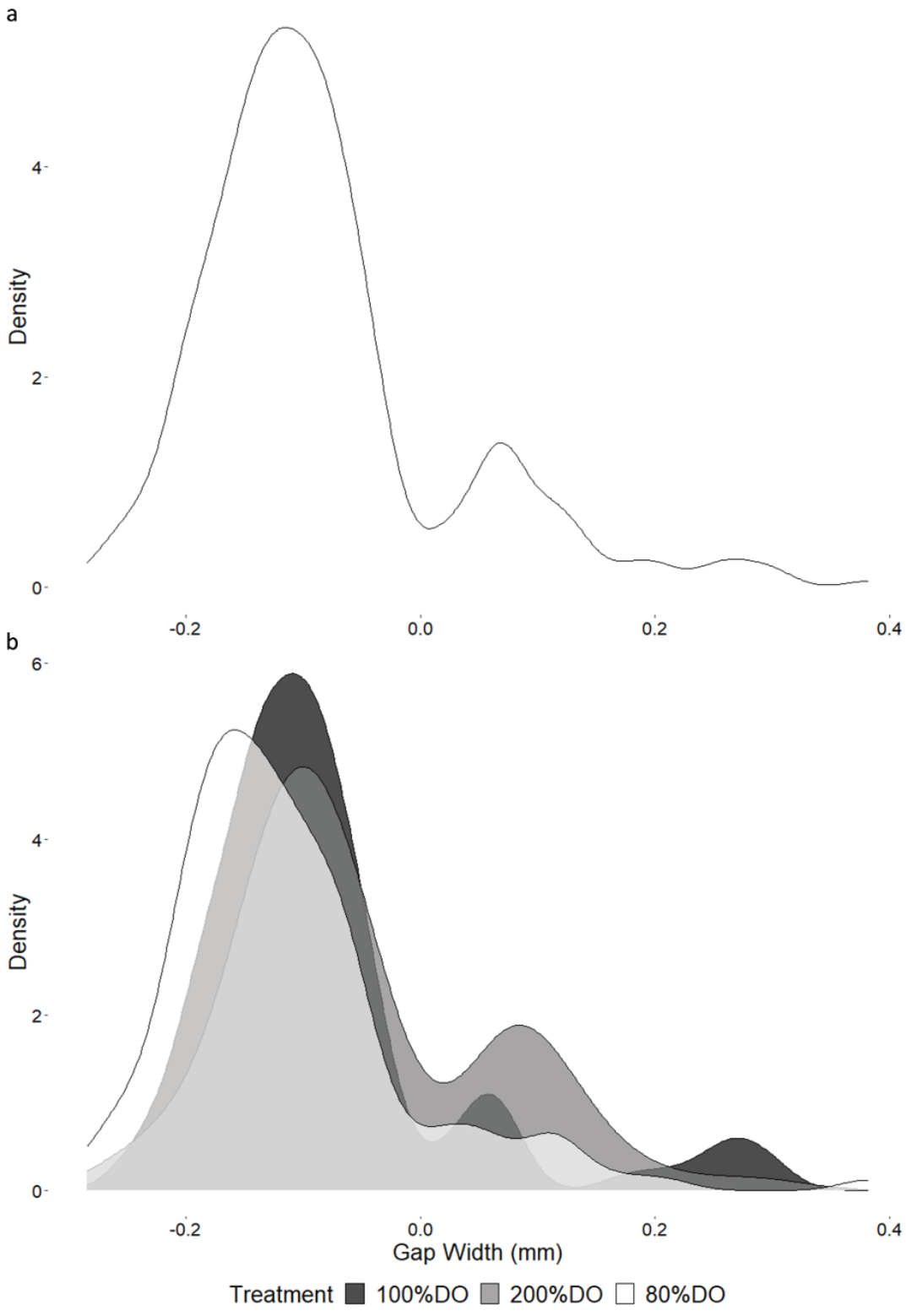

Figure 4 – Density distribution of gap width values. **a**. bimodal distribution of specimens with normal (left peak) and deformed (right peak) opercula. **b**. density distributions of gap width, coloured according to treatment.

displaying negative gap values. PC2 explained 16% of the variation, separating specimens based on their opercular morphotype (Fig. 5). Factor loadings for this PC indicated that a change in GW is nearly independent from the overall size of the fish, as can be seen in Fig. 7, where the factor GW is projected almost perpendicularly onto the other factors. PC3 contained 3.7% of the variation, mainly explained by relative snout length. Again, no clustering according to treatment was detected.

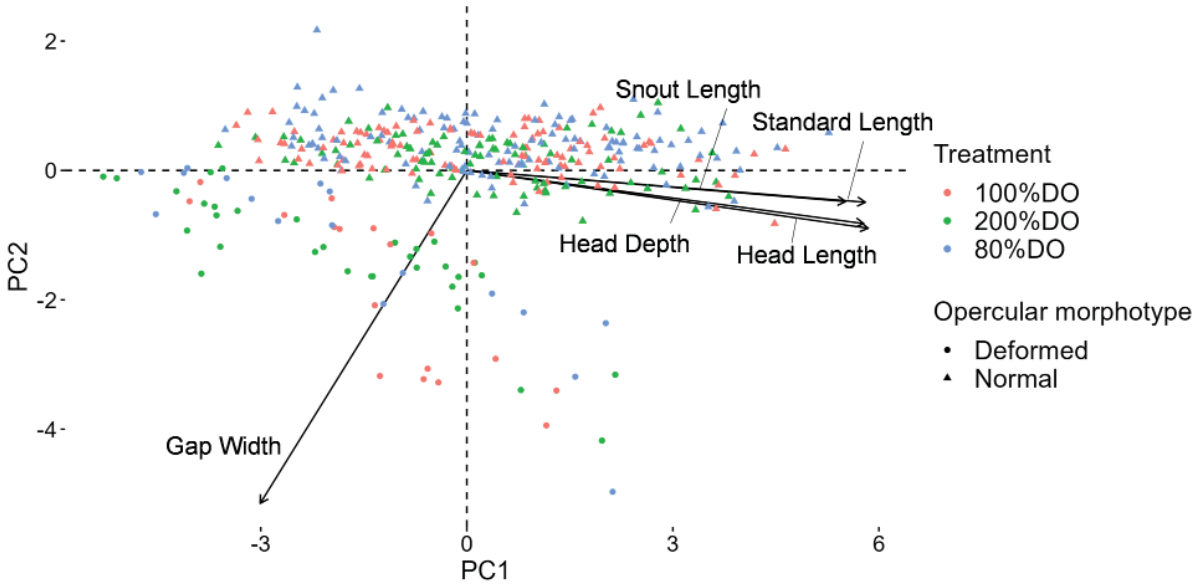

Figure 5 – PCA biplot (PC1 vs PC2) of all body measurements (gap width included) on specimens of 48 and 55 DPH. Colour coding is according to treatment.

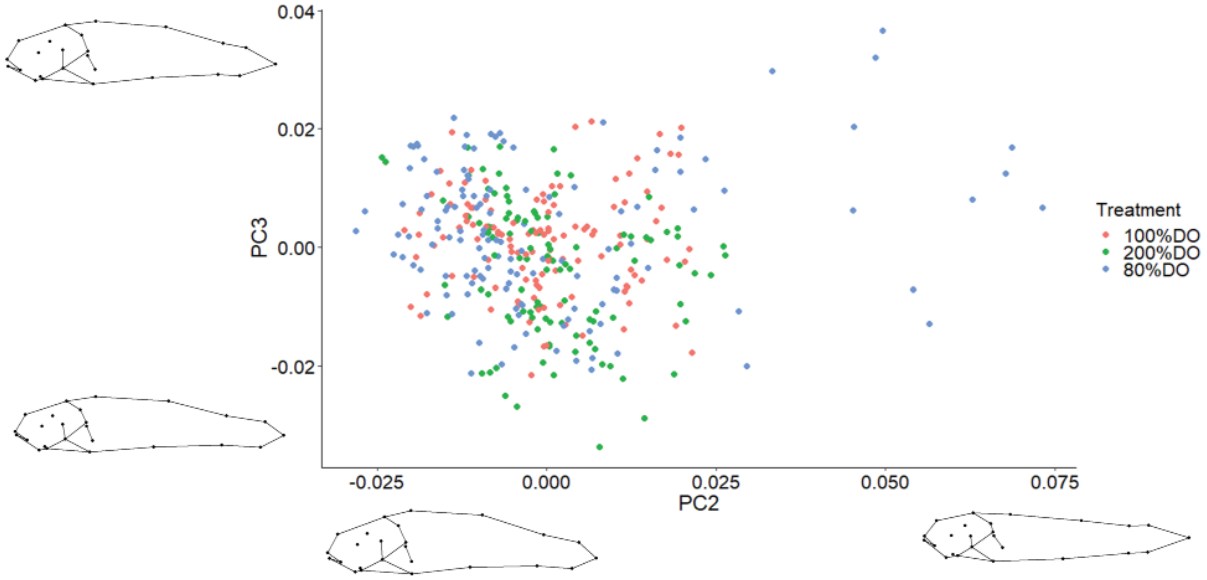

Figure 6 – Biplot of PC2 vs PC3 of the landmark data, with colour coding according to treatment. Shapes represent the landmark configurations that correspond with the minimum and the maximum PC scores.

Body shape

The digitisation error was 19.70%, and confirms that the individual specimens can be distinguished from each other with this approach. The orientation error was marginally negative (-1.52%), inferring that this error was negligibly small. A PCA with broken-stick on the 48 and 55 DPH samples (n = 191) recovered the first three PCs as relevant, explaining 74.03% of the shape variation (Fig. 6). PC1 (45.39%) characterized a dorsoventral curving of the body, probably a fixation artefact. This PC is thus omitted in further graphical representations. PC2 (18.68%), represented variation in the height of the abdomen, accompanied by a slight downward bending of the tail region (Fig. 6). The few 80% DO specimens with a higher PC2 score differed from the others in having signs of scoliotic deformity. PC3 (9.96%) revealed variation in the height of the head and abdominal region, and overall size of the tail region (Fig. 6). No clustering according to treatment or opercular morphotype was found.

The Procrustes linear model explained 25.7% of the body shape variation, indicating a low fit with SL and treatment. Most of the explained variation was due to SL ($R^2 = 23.4\%$, $p = 0.001$) suggesting a weak size allometry, while treatment explained very little shape variation ($R^2 = 2.3\%$, $p = 0.001$). This allometry mainly involved an elongation of the skull, a ventral expansion of the branchiostegal region, a heightening of the abdominal region, and a reduction of the tail region as overall size increased. As opercular morphotype showed no significant effect, it was left out of the final model. A pairwise comparison between mean treatment group shapes showed that only the 200% DO shapes differed significantly from that of the other two treatments ($p = 0.001$ for both).

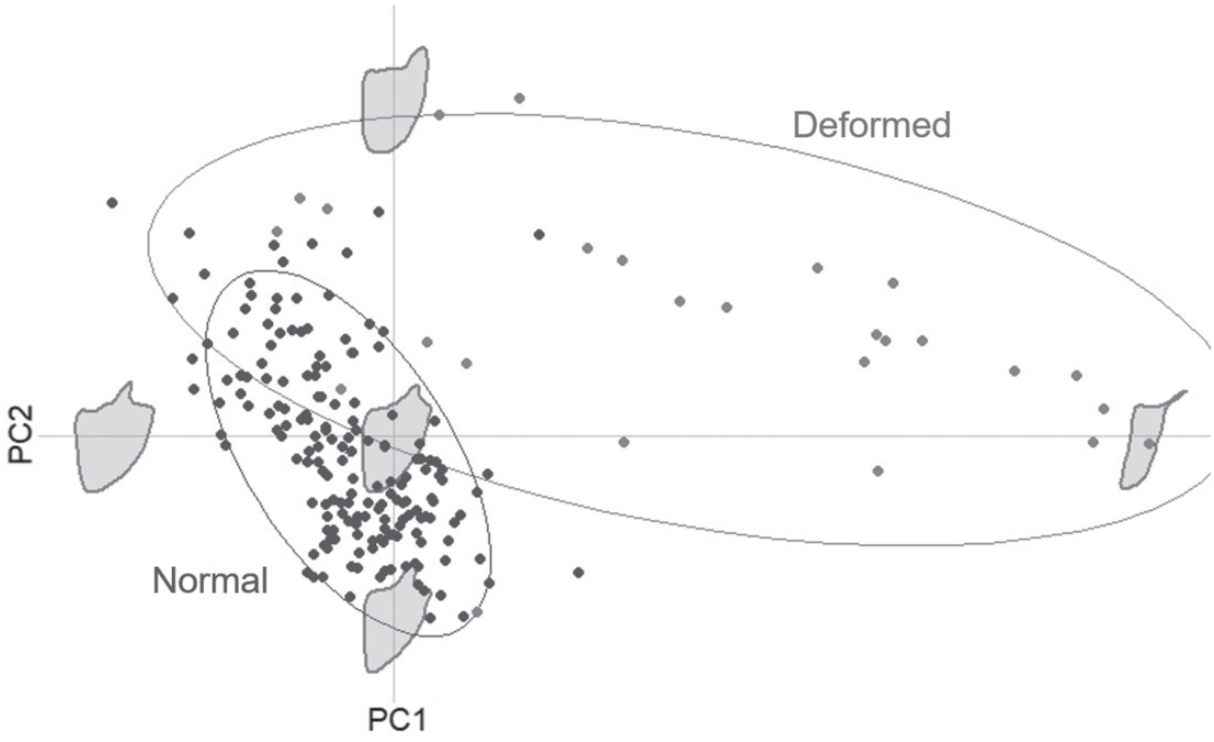

Figure 7 – Biplot of PC1 vs PC2 on opercular outline data, colour coded according to opercular morphotype (95% confidence ellipses added). Black = normal shape; grey = deformed shape. The shapes on the axes represent the average shape (centre), and the shapes on the extremes of both PCs.

Opercular shape

A total of 202 opercula across the three treatments were analysed, where 11 harmonics covered 99% of the shape variation. The broken-stick analysis recovered the first four PCs as relevant, explaining 82.83% of the opercular shape variation. PC1 (46.38%) reflected variation in an antero-posterior position of the caudal edge of the operculum, associated with the level of deformation as defined by GW. PC2 (17.75%) also represented variation in the opercular width (to a lesser degree than PC1), but also included variation in the curvature of the dorsocaudal region (Fig. 7). PC3 and PC4 (10.62% and 8.08%, respectively) covered variation in the overall shape, magnitude and acuteness of the dorsal protrusions. Interestingly, not all specimens labelled as deformed (positive GW values) had an opercular shape deviating from the normal one (Fig. 7). No clustering according to treatment was detected (not shown). Variation among normal opercular morphotypes was similar for all treatments, with 95% confidence ellipses overlapping strongly, while the variation of deformed morphotypes was larger in 200% DO, but limited in 80% DO.

MANOVA test results revealed that normal opercula significantly differed from deformed ones ($p < 0.001$). The mean shapes of both morphotypes are represented in Fig. 8a. However, care should be taken when interpreting this figure. Shapes were superimposed so that their centroid points overlapped, giving the impression that a deformed opercle changed in shape on both the rostral and the caudal side, while it was in fact only at the latter. Thus, for a correct interpretation, the frontal edges of both opercular morphotypes should be aligned, revealing an even stronger shape change at the caudal side (Fig. 8b).

Treatment affected opercular shape ($p < 0.001$), but also its interaction with morphotype, indicating that opercular bones of the same morphotype did differ between treatments. A pairwise comparison per morphotype revealed that the shapes of the normal opercular morphotypes differed statistically from each other across treatments, while the deformed ones did not. The level of these shape differences across the normal morphotypes was very subtle, with the shape of the dorsal protrusion under 100% DO being slightly different from the other treatments (Fig. 9a). The deformed morphotypes on the other hand, expressed a more pronounced, but non-significant difference across treatments (Fig. 9b). This was likely due to the low number of specimens. Most severe malformations appeared in the 80% DO treatment.

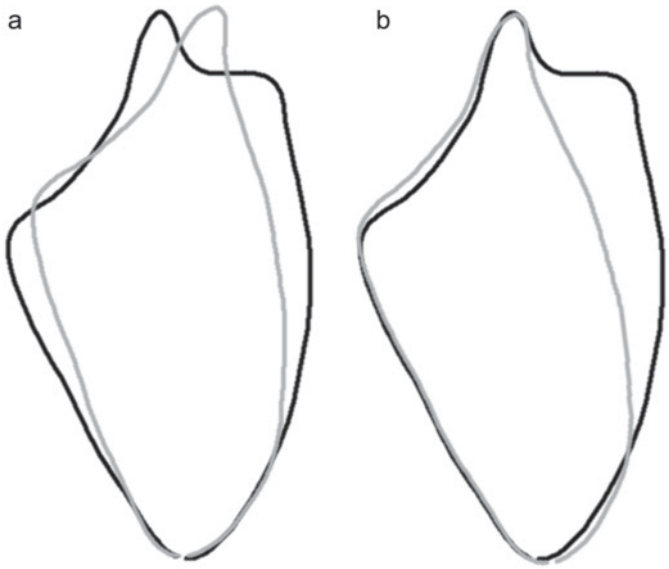

Figure 8 – Comparison of mean shapes for both opercular morphotypes. Black = normal shape, grey = deformed shape. **a**. Shape superimposition based on overlapping centroid points. **b**. Manually adjusted shape superimposition resulting in a leftward tilt of the deformed opercle, revealing a shape shift almost exclusively at the distal region.

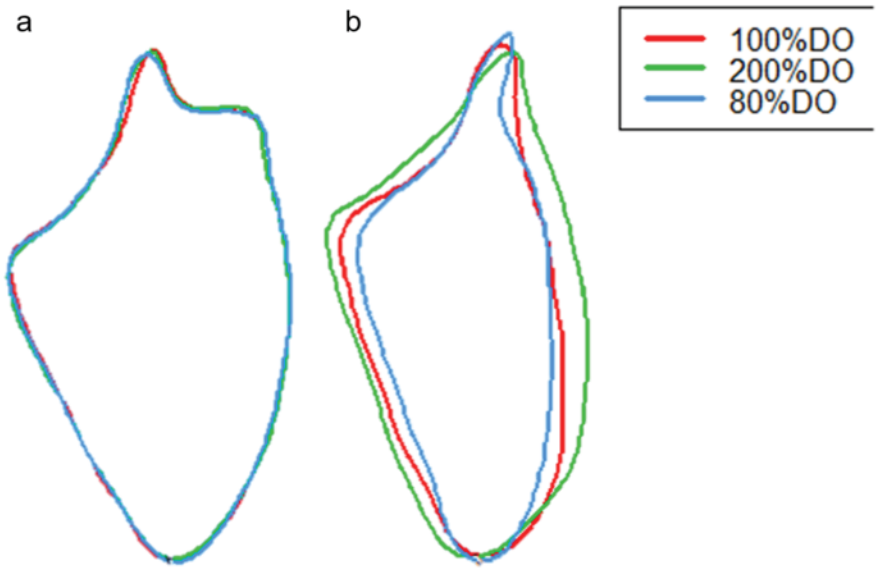

Figure 9 – Comparison between mean normal (a) and mean deformed (b) shapes for each treatment.

Morphological description of deformed opercula

Deformed opercles with a gap between the distal opercular border and the cleithrum exposed a large part of the gill cavity. This gap was the result of an inward folding or curling of the caudal region of the operculum (Fig. 10). In one individual, the opercle was folded to the outside, but with its caudal tip folded inwards. Severe deformations involved a more acute and spiralling dorsal process. The surrounding suboperculum and the caudal tips of the branchiostegal rays also showed deformations and followed the same pattern and direction of folding as of the opercular bone.

Discussion

Oxygen treatment & mechanical loading

By altering gill ventilation through the exposure to varying DO levels, we expected that this would lead to an altered mechanical loading by the opercular muscles onto the medial crest of the opercular bone (where the adductor muscle inserts). We observed deformations mainly in the dorsocaudal and caudal region of the opercular bone (Fig. 7). Since this bone ossifies in a rostro-caudal direction (Faustino & Power 2001; Kimmel *et al.* 2010), the caudal region remains unossified for a relative long time, making it more susceptible to bending as it pushes against the surrounding water. The observed deformations thus match opercular regions, where altered mechanical loading due to changes in gill ventilation would be expected. No deformity was detected at the processus dorsalis (where the abductor muscle inserts), lying at the proximal side of the opercle (Fig. 10). Alternately, the results of the GW measurements and the opercular shape analysis indicate a non-significant difference between the treatments. In this study, neither of the two approaches allows confirmation that opercular deformations are a direct cause of a mechanical stressor or that the observed deformations are the result of a difference in mechanical stress (ventilation rate). Nonetheless, an increased opercular abduction could still be indirectly involved in the deformation of the dorsocaudal part of the operculum, due to the negative hydrodynamic pressure generated by the so-called suction pump system (Hughes 1960). The actual response of the opercular ventilation rate to the three DO concentrations (and altered mechanical loading) was not quantified

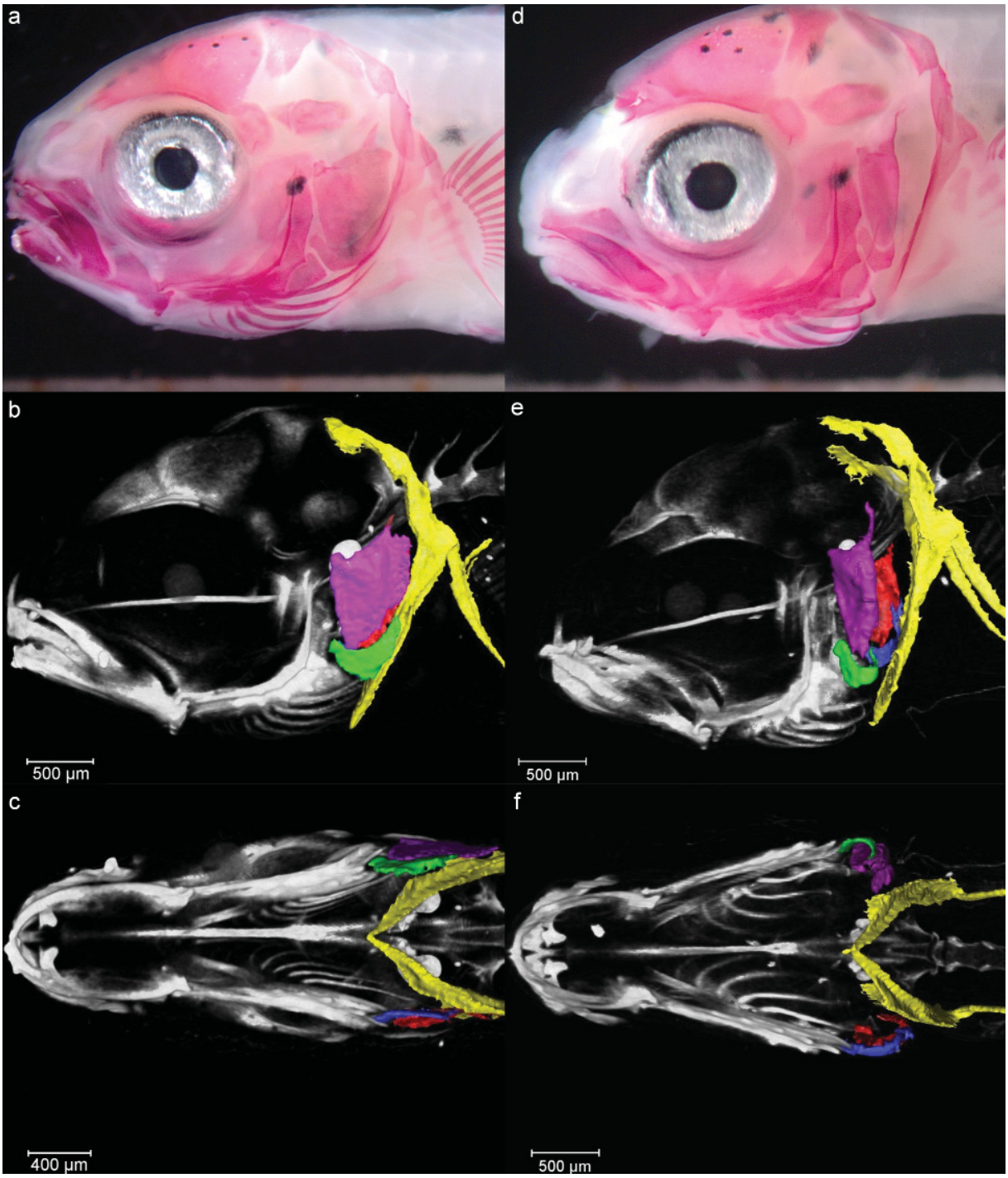

Figure 10 – 2D and 3D images of a 48 DPH mildly (a-c) and heavily deformed (d-f) specimen of *Sparus aurata*. Figures b, c, e and f are 3D reconstructions based on µCT-scans. Figures b and e are lateral views, c and f are ventral views. Colour code for the structures: yellow = pectoral girdle; purple = left opercular bone; green = left subopercular bone; red = right opercular bone; blue = right subopercular bone.

in this study. Monitoring this effect directly and including more extreme DO concentrations could further validate our hypothesis. Smaller individuals such as fish larvae could also be monitored through macroscopic close-up observations. Small electronic sensors such as miniaturized accelerometers attached to the opercula, have been used before to monitor the respiratory frequency in larger fish (MARTOS-SITCHA *et al.* 2019).

Oxygen treatment & incidence of deformation

In this study, 27.2% of the fish displayed opercular deformations (Table 2), where in literature the frequency ranges from 6.3% to 27% and even up to 80% (ANDRADES *et al.* 1996; DIVANACH *et al.* 1996; ORTIZ-DELGADO *et al.* 2014). Differences in prevalence could be attributed to changes in fish husbandry over the last decades (KOUMOUNDOUROS *et al.* 2010; PRESTINICOLA *et al.* 2014). We observed deformed opercula in all treatments, with those under 80% DO conditions being the most severe in terms of opercular shape (Fig. 9). No difference was found in the number of left- or right-deformed opercula (Table 2), which contrasts with the directional asymmetry observed by VERHAEGEN *et al.* (2007) but is in line with the observations by KOUMOUNDOUROS *et al.* (1997), GALEOTTI *et al.* (2000) and BERALDO *et al.* (2003).

In terms of GW, the prevalence of deformities in each treatment drops between 48 and 55 DPH (Table 2). It is unlikely that this decline is due to the mortality of deformed fish, as the relative mortality in this period is not sufficiently high (0.2–0.35%) to justify the drop in total fish with deformed opercular bones. Alternately, some deformed animals might have recovered from their anomaly, a phenomenon that has been observed before in older individuals (BERALDO & CANAVESE 2011). Within such a short time span, recovery of a deformed gill cover would only be achievable for individuals with a very mild deformation (low positive GW value). This would be in line with our observations as the average relative GW value of a deformed morphotype is larger at 55 DPH than at 48 DPH (Table 2). Regardless, the 200% DO treatment results in the highest prevalence of opercular deformities in both age groups.

We hypothesized that hypoxia would lead to an increased prevalence of opercular deformities, yet this treatment yielded similar results as normoxic conditions (Table 2). The 80% DO treatment, the suggested minimum O_2 level for appropriate rearing of gilthead sea bream, may not have been sufficiently low to trigger a change in ventilation (PAVLIDIS & MYLONAS 2011). As we could not quantify actual changes in ventilation rates, we cannot corroborate this at this point. For both the closely related common dentex (VALVERDE *et al.* 2006) and sharpsnout sea bream (CEREZO & GARCÍA GARCÍA 2004), DO levels below 70% are sub-optimal and increase ventilation frequency. Compared to the hypoxia threshold level for gilthead sea bream, this indicates interspecific differences in the minimum rearing DO level, even for closely related species. For gilthead sea bream, the % O_2 saturation where the fish can no longer maintain their metabolism, is observed to be around 35% O_2 at 20°C (REMEN *et al.* 2015). All these arguments are in support of the conclusion that in our experiment, 80% DO was not sufficiently low to trigger substantial changes in gill ventilation.

Under hyperoxia, we expected less fish with deformed opercula than under normoxia but observed the opposite (Table 2). Negative consequences of hyperoxia can impact respiratory structures, including damage to the branchial lamellae due to oedema formation (WU *et al.* 2016). A resulting impaired functional performance of the gills related to oxygen uptake could then trigger a compensatory increased ventilation frequency, which in turn would increase the mechanical loading on the gill cover. Unexpectedly, and under those assumptions (as we could not verify actual changes in ventilation), the results from the hyperoxic treatment in this study may provide support for our hypothesis of mechanically induced opercular deformities. An integrated approach monitoring DO levels in the blood and quantifying ventilation frequency could provide conclusive evidence for this. More practically, our

results also indicate not to use oversaturated oxygen levels for the rearing of larval and juvenile sea bream.

Although GW is an easily recognizable and measurable feature, it proves no unambiguous approach, as the opercular shape analysis indicates that not all specimens labelled as 'deformed' based on GW value show a deformed opercular phenotype (Fig. 7). Both approaches represent a different aspect of opercular deformation: GW is a proxy for the level of gill exposure, while the geometric morphometric approach only reveals the 2D variation in opercular shape from a lateral point of view. Further studies on opercular deformations could benefit from a combination of both approaches. Nonetheless, a visual observation of the degree of gill exposure through staining proves a rapid and easily applicable approach in a practical environment. Additionally, the level of gill exposure (as seen macroscopically) greatly affects the market value and product image and is therefore a critical feature to monitor. The association of opercular deformations with transformation of nearby structures, such as the subopercular bone and branchiostegal rays observed in this study, confirms the findings of other studies (Koumoundouros *et al.* 1997; Beraldo *et al.* 2003; Verhaegen *et al.* 2007; Thuong *et al.* 2017). The actual phenotypic alteration is not restricted to a shortening of the subopercular bone (as would be observed when only considering a lateral view) but also involves a similar inward folding as in the opercular bone. Considering the close connection between those bones, both structurally and functionally (all are involved in respiratory ventilation), there could still be a mechanically related deformation in all of them.

The current study focused solely on a possible mechanical effect of oxygen treatment on opercular ventilation, though different DO levels can lead to other consequences as well. When experiencing reduced oxygen levels, such as hypoxic water or after exercise, fish may rely on alternative respiratory ventilation modes. During very active ventilation, the pectoral girdle (via the hypaxial muscles) and the ventral branchial muscles are recruited to assist in active jaw abduction (Taylor *et al*. 2006). Many fish species also switch to surface-breathing (Domenici *et al*. 2013). Under hypoxic conditions, fish may switch to anaerobic metabolism and allocate more energy into respiration. This often causes a reduction in locomotory activity and feed ingestion, in turn reducing growth (Magnoni *et al*. 2018). Also direct effects of oxygen levels on bone development cannot be excluded as a causal factor for the observed deformities. Under hypoxic conditions, mesenchymal stem cells preferentially differentiate into chondrocytes rather than osteoblasts (Simon & Keith 2008), whereas even a brief exposure to extreme hypoxia inhibits osteoblast differentiation (Utting *et al.* 2006). This cell differentiation is influenced by the hypoxia-inducible factor 1α (HIF-1α, a transcription factor that mediates the adaptive response of cells to hypoxia). Elevated levels of HIF-1α transcripts were observed in a marine teleost exposed to 55% DO and lower (Rahman & Thomas 2007). However, these concentrations are far below the ones applied in the current study, and it could thus not be verified to what degree HIF-1α could also explain aspects of the observed deformations.

Oxygen treatment and size

The body size of the 'normal' opercular morphotype was slightly, but significantly larger than of the 'deformed' ones at 48 and 55 DPH (Table 3). Verhaegen *et al.* (2007) distinguished a similar pattern at 65 DPH, suggesting that the size effect arises and is retained during some time, and is likely the result of an impaired ventilation. In contrast, the DO treatments in our study did not result in overall size effects after 34 DPH (Table 3). Hypoxic conditions are known to stagnate growth in fish, which is primarily the result of a reduced food intake and an impaired food conversion efficiency. However, the specific level of hypoxia-related growth reduction varies among species and depends on the oxygen affinity and the cardiorespiratory robustness of the fish (Wang *et al.* 2009). The fact that growth was not sufficiently reduced at 80% DO (Fig. 2 and Table 3) corroborates the conclusion that this oxygen level is not sufficiently low to cause a negative effect on sea bream growth. No growth effect was detected in

the hyperoxic conditions (200% DO) either (Fig. 2 and Table 3). Hyperoxia is known to have little to no effect on fish growth, as feed conversion and metabolism seem unaffected (McArley *et al*. 2021). Any negative impacts are more likely caused by an increased oxygen gas pressure (e.g., gas bubble disease) than a rise in DO levels. A significant difference in body shape was found between 200% DO and the other treatments , although mean shape did not differ markedly (Fig. 6). The range of DO levels used in this study thus has no severe impact on the overall shape of gilthead sea bream juveniles. This observation does not exclude these oxygen levels from having alternate negative effects that are relevant for both fish welfare and for aquaculture production.

Conclusion

This study examined the possible association between mechanical loading and opercular deformities. Results revealed that neither of our expectations on the prevalence of deformed opercula under hypoxic and hyperoxic conditions could be confirmed. Using GW as a single measure of opercular deformation proved useful, but it is no unambiguous proxy. A combination with opercular shape analysis would benefit future studies. Indirect evidence suggests that increased ventilatory frequency and volume, whether under hypoxic or even hyperoxic conditions, could trigger an increased opercular muscle contraction activity and associated mechanical loading on the opercular and associated bones, leading to observed deformations mainly on the dorsocaudal region of the opercular bone. The direct effects of the different DO levels on the ventilation rate of larval and early juvenile seabream should be investigated to further corroborate our hypothesis. More insights into the spatial distribution of mechanical loading patterns and the direct effect on bone morphogenesis at muscle insertion sites are required to allow a more reliable testing of the impact of mechanical loading as a direct causal factor of abnormal skeletogenesis of opercula.

Relevant declarations of interest

The authors have no conflict of interest to declare.

Acknowledgements

We are especially grateful to the INVE hatchery (Maricoltura di Rosignano Solvay) for growing and providing the specimens.

References

Adams D.C. & Otárola-Castillo E. (2013). geomorph: an R package for the collection and analysis of geometric morphometric shape data. *Methods in Ecology and Evolution* 4: 393–399. https://doi.org/10.1111/2041-210X.12035

Adams D., Collyer M. & Kaliontzopoulou A. (2018). *Geometric Morphometric Analyses of 2D/3D Landmark Data*. Available from https://rdrr.io/cran/geomorph/ [accessed 17 July 2023].

Andrades J.A., Becerra J. & Fernandez-Llebrez P. (1996). Skeletal deformities in larval, juvenile and adult stages of cultured gilthead sea bream (*Sparus aurata* L.). *Aquaculture* 141: 1–11. https://doi.org/10.1016/0044-8486(95)01226-5

Atkins A., Milgram J., Weiner S. & Shahar R. (2015). The response of anosteocytic bone to controlled loading. *Journal of Experimental Biology* 218: 3559–3569. https://doi.org/10.1242/jeb.124073

Beraldo, P. & Canavese, B. (2011). Recovery of opercular anomalies in gilthead sea bream, *Sparus aurata* L.: morphological and morphometric analysis. *Journal of Fish Diseases* 34: 21–30. https://doi.org/10.1111/j.1365-2761.2010.01206.x

Beraldo P., Pinosa M., Tibaldi E. & Canavese B. (2003). Abnormalities of the operculum in gilthead sea bream (*Sparus aurata*): morphological description. *Aquaculture* 220: 89–99. https://doi.org/10.1016/S0044-8486(02)00416-7

Boglione C., Gisbert E., Gavaia P. E., Witten P., Moren M., Fontagné S. & Koumoundouros G. (2013). Skeletal anomalies in reared European fish larvae and juveniles. Part 2: main typologies, occurrences and causative factors. *Reviews in Aquaculture* 5: S121–S167. https://doi.org/10.1111/raq.12016

Bonewald L.F. (2011). The amazing osteocyte. *Journal of Bone and Mineral Research* 26: 229–238. https://doi.org/10.1002/jbmr.320

Bonhomme V., Picq S., Gaucherel C. & Claude J. (2014). Momocs: outline analysis using R. *Journal of Statistical Software* 56: 1–24. https://doi.org/10.18637/jss.v056.i13

Cerezo J. & García García B. (2004). The effects of oxygen levels on oxygen consumption, survival and ventilatory frequency of sharpsnout sea bream (*Diplodus puntazzo* Gmelin, 1789) at different conditions of temperature and fish weight. *Journal of Applied Ichthyology* 20: 488–492. https://doi.org/10.1111/j.1439-0426.2004.00601.x

Chatain B. (1994). Abnormal swimbladder development and lordosis in sea bass (*Dicentrarchus labrax*) and sea bream (*Sparus auratus*). *Aquaculture* 119: 371–379. https://doi.org/10.1016/0044-8486(94)90301-8

Divanach P.B.C.M.B., Boglione C., Menu B., Koumoundouros G., Kentouri M. & Cataudella S. (1996). Abnormalities in finfish mariculture: an overview of the problem, causes and solutions. *Special Publication/European Aquaculture Society* 45–66.

Domenici P., Herbert N.A., Lefrançois C., Steffensen J.F. & McKenzie D.J. (2013). The effect of hypoxia on fish swimming performance and behaviour. *Swimming Physiology of Fish: Towards Using Exercise to Farm a Fit Fish in Sustainable Aquaculture* 129–159. https://doi.org/10.1007/978-3-642-31049-2_6

Ekanayake S. & Hall B. K. (1988). Ultrastructure of the osteogenesis of acellular vertebral bone in the Japanese medaka, *Oryzias latipes* (Teleostei, Cyprinidontidae). *American Journal of Anatomy* 182: 241–249. https://doi.org/10.1002/aja.1001820305

EUMOFA (2022). *The EU Fish Market*. Luxembourg: Publications Office of the European Union. https://doi.org/10.2771/716731

Faustino M. & Power D.M. (2001). Osteologic development of the viscerocranial skeleton in sea bream: alternative ossification strategies in teleost fish. *Journal of Fish Biology* 58: 537–572. https://doi.org/10.1111/j.1095-8649.2001.tb02272.x

Fernández I., Darias M., Andree K.B., Mazurais D., Zambonino-Infante J.L. & Gisbert E. (2011). Coordinated gene expression during gilthead sea bream skeletogenesis and its disruption by nutritional hypervitaminosis A. *BMC Developmental Biology* 11: 7. https://doi.org/10.1186/1471-213X-11-7

Ferrer M.A., Calduch-Giner J.A., Díaz M., Sosa J., Rosell-Moll E., Abril J.S.,Sosa G.S., Delgado T.B., Carmona C., Martos-Sitcha J.A., Cabruja E., Afonso J.M., Vega A., Lozano M., Montiel-Nelson J.A. & Pérez-Sánchez J. (2020). From operculum and body tail movements to different coupling of physical activity and respiratory frequency in farmed gilthead sea bream and

European sea bass. Insights on aquaculture biosensing. *Computers and Electronics in Agriculture* 175: 105531. https://doi.org/10.1016/j.compag.2020.105531

Galeotti M., Beraldo P., De Dominis S., D'angelo L., Ballestrazzi R., Musetti R., Pizzolito S. & Pinosa M. (2000). A preliminary histological and ultrastructural study of opercular anomalies in gilthead sea bream larvae (*Sparus aurata*). *Fish Physiology and Biochemistry* 22: 151–157. https://doi.org/10.1023/A:1007883008076

García-Celdrán M., Ramis G., Manchado M., Estévez A., Afonso J. M., María-Dolores E., Peñalver J. & Armero E. (2015). Estimates of heritabilities and genetic correlations of growth and external skeletal deformities at different ages in a reared gilthead sea bream (*Sparus aurata* L.) population sourced from three broodstocks along the Spanish coasts. *Aquaculture* 445: 33–41. https://doi.org/10.1016/j.aquaculture.2015.04.006

García-Celdrán M., Cutáková Z., Ramis G., Estévez A., Manchado M., Navarro A., María-Dolores E., Peñalver J., Sánchez J.A. & Armero E. (2016). Estimates of heritabilities and genetic correlations of skeletal deformities and uninflated swimbladder in a reared gilthead sea bream (*Sparus aurata* L.) juvenile population sourced from three broodstocks along the Spanish coasts. *Aquaculture* 464: 601–608. https://doi.org/10.1016/j.aquaculture.2016.08.004

Georgakopoulou E., Katharios P., Divanach P. & Koumoundouros G. (2010). Effect of temperature on the development of skeletal deformities in Gilthead seabream (*Sparus aurata* Linnaeus, 1758). *Aquaculture* 308: 13–19. https://doi.org/10.1016/j.aquaculture.2010.08.006

Hughes G.M. (1960). A comparative study of gill ventilation in marine teleosts. *Journal of Experimental Biology* 37: 28–45. https://doi.org/10.1242/jeb.37.1.28

Kimmel C.B., DeLaurier A., Ullmann B., Dowd J. & McFadden M. (2010). Modes of developmental outgrowth and shaping of a craniofacial bone in zebrafish. *PloS ONE* 5: e9475. https://doi.org/10.1371/journal.pone.0009475

Koumoundouros G. (2010). Morpho-anatomical abnormalities in Mediterranean marine aquaculture. *Recent Advances in Aquaculture Research* 66: 125–148.

Koumoundouros G., Oran G., Divanach P., Stefanakis S. & Kentouri M. (1997). The opercular complex deformity in intensive gilthead sea bream (*Sparus aurata* L.) larviculture. Moment of apparition and description. *Aquaculture* 156: 165–177. https://doi.org/10.1016/S0044-8486(97)89294-0

Kranenbarg S., Waarsing J.H., Muller M., Weinans H. & van Leeuwen J.L. (2005). Lordotic vertebrae in sea bass (*Dicentrarchus labrax* L.) are adapted to increased loads. *Journal of Biomechanics* 38: 1239–1246. https://doi.org/10.1016/j.jbiomech.2004.06.011

Kuhl F.P. & Giardina C.R. (1982). Elliptic Fourier features of a closed contour. *Computer Graphics and Image Processing* 18: 236–258. https://doi.org/10.1016/0146-664X(82)90034-X

Kuroki M., Okamura A., Takeuchi A. & Tsukamoto K. (2016). Effect of water current on the body size and occurrence of deformities in reared Japanese eel leptocephali and glass eels. *Fisheries Science* 82: 941–951. https://doi.org/10.1007/s12562-016-1015-7

MacArthur R.H. (1957). On the relative abundance of bird species. *Proceedings of the National Academy of Sciences* 43: 293–295. https://doi.org/10.1073/pnas.43.3.293

Magnoni L.J., Eding E., Leguen I., Prunet P., Geurden I., Ozório R.O. & Schrama J.W. (2018). Hypoxia, but not an electrolyte-imbalanced diet, reduces feed intake, growth and oxygen consumption in rainbow trout (*Oncorhynchus mykiss*). *Scientific Reports* 8: 1–14. https://doi.org/10.1038/s41598-018-23352-z

Martos-Sitcha J.A., Sosa J., Ramos-Valido D., Bravo F.J., Carmona-Duarte C., Gomes H.L., Calduch-Giner J.À., Cabruja E., Vega A., Ferrer M.Á., Lozano M., Montiel-Nelson J.A., Afonso J.M. & Pérez-Sánchez J. (2019). Ultra-low power sensor devices for monitoring physical activity and respiratory frequency in farmed fish. *Frontiers in Physiology* 10: 667. https://doi.org/10.3389/fphys.2019.00667

McArley T.J. Sandblom E. & Herbert N.A. (2021). Fish and hyperoxia—from cardiorespiratory and biochemical adjustments to aquaculture and ecophysiology implications. *Fish and Fisheries* 22: 324–355. https://doi.org/10.1111/faf.12522

Morel C., Adriaens D., Boone M., De Wolf T., Van Hoorebeke L. & Sorgeloos P. (2010). Visualizing mineralization in deformed opercular bones of larval gilthead sea bream (*Sparus aurata*). *Journal of Applied Ichthyology* 26: 278–279. https://doi.org/10.1111/j.1439-0426.2010.01420.x

Noble C., Jones H.A.C., Damsgård B., Flood M.J., Midling K.Ø., Roque A., Sæther B.-S. & Cottee S.Y. (2012). Injuries and deformities in fish: their potential impacts upon aquacultural production and welfare. *Fish Physiology and Biochemistry* 38: 61–83. https://doi.org/10.1007/s10695-011-9557-1

Ofer L., Dumont M., Rack A., Zaslansky P. & Shahar R. (2019). New insights into the process of osteogenesis of anosteocytic bone. *Bone* 125: 61–73. https://doi.org/10.1016/j.bone.2019.05.013

Ortiz-Delgado J.B., Fernández I., Sarasquete C. & Gisbert E. (2014). Normal and histopathological organization of the opercular bone and vertebrae in gilthead sea bream *Sparus aurata*. *Aquatic Biology* 21: 67–84. https://doi.org/10.3354/ab00568

Paperna I., Ross B., Colorni A. & Colorni B. (1980). Diseases of marine fish cultured in Eilat mariculture project based at the Gulf of Aqaba, Red Sea. *Studies and Reviews-General Fisheries Council for the Mediterranean (FAO)* 57.

Pavlidis M.A. & Mylonas C.C. (2011). *Sparidae: Biology and Aquaculture of Gilthead Sea Bream and Other Species*. John Wiley & Sons.

Perry S.F., Jonz M.G. & Gilmour K.M. (2009). Oxygen sensing and the hypoxic ventilatory response. *Fish Physiology* 27: 193–253. https://doi.org/10.1016/S1546-5098(08)00005-8

Prestinicola L., Boglione C. & Cataudella S. (2014). Relationship between uninflated swim bladder and skeletal anomalies in reared gilthead seabream (*Sparus aurata*). *Aquaculture* 432: 462–469. https://doi.org/10.1016/j.aquaculture.2014.06.020

R Core Team (2018). *R: A Language and Environment for Statistical Computing*. R Foundation for Statistical Computing, Vienna, Austria.

Rahman M.S. & Thomas P. (2007). Molecular cloning, characterization and expression of two hypoxia-inducible factor alpha subunits, HIF-1alpha and HIF-2alpha, in a hypoxia-tolerant marine teleost, Atlantic croaker (*Micropogonias undulatus*). *Gene* 396: 273–282. https://doi.org/10.1016/j.gene.2007.03.009

Remen M., Nederlof M.A., Folkedal O., Thorsheim G., Sitjà-Bobadilla A., Pérez-Sánchez J., Oppedal F. & Olsen R.E. (2015). Effect of temperature on the metabolism, behaviour and oxygen requirements of *Sparus aurata*. *Aquaculture Environment Interactions* 7: 115–123. https://doi.org/10.3354/aei00141

Rohlf F.J. (2015). The tps series of software. *Hystrix* 26. https://doi.org/10.4404/hystrix-26.1-11264

Rohlf F.J. & Bookstein F.L. (1990). *Proceedings of the Michigan Morphometrics Workshop*. University of Michigan Museum of Zoology.

ROHLF F.J. & SLICE D. (1990). Extensions of the Procrustes method for the optimal superimposition of landmarks. *Systematic Biology* 39: 40–59. https://doi.org/10.2307/2992207

ROO J., SOCORRO J. & IZQUIERDO M.S. (2010). Effect of rearing techniques on skeletal deformities and osteological development in red porgy *Pagrus pagrus* (Linnaeus, 1758) larvae. *Journal of Applied Ichthyology* 26: 372–376. https://doi.org/10.1111/j.1439-0426.2010.01437.x

SCHINDELIN J., ARGANDA-CARRERAS I., FRISE E., KAYNIG V., LONGAIR M., PIETZSCH T., PREIBISCH S., RUEDEN C., SAALFELD S., SCHMID B., TINEVEZ J.-Y., WHITE D.J., HARTENSTEIN V., ELICEIRI K., TOMANCAK P. & TINEVEZ J.Y. (2012). Fiji: an open-source platform for biological-image analysis. *Nature Methods* 9: 676. https://doi.org/10.1038/nmeth.2019

SCHNEIDER C.A., RASBAND W.S. & ELICEIRI K.W. (2012). NIH Image to ImageJ: 25 years of image analysis. *Nature Methods* 9: 671. https://doi.org/10.1038/nmeth.2089

SFAKIANAKIS D.G., RENIERI E., KENTOURI M. & TSATSAKIS A.M. (2015). Effect of heavy metals on fish larvae deformities: a review. *Environmental research* 137: 246–255. https://doi.org/10.1016/j.envres.2014.12.014

SHAHAR R. & DEAN M. N. (2013). The enigmas of bone without osteocytes. *BoneKEy Reports* 2. https://doi.org/10.1038/bonekey.2013.77

SIMON M.C. & KEITH B. (2008). The role of oxygen availability in embryonic development and stem cell function. *Nature Reviews Molecular Cell Biology* 9: 285. https://doi.org/10.1038/nrm2354

TAYLOR E.W., CAMPBELL H.A., LEVINGS J.J., YOUNG M.J., BUTLER P.J. & EGGINTON S. (2006). Coupling of the respiratory rhythm in fish with activity in hypobranchial nerves and with heartbeat. *Physiological and Biochemical Zoology* 79: 1000–1009. https://doi.org/10.1086/507663

THUONG N.P., VERSTRAETEN B., KEGEL B.D., CHRISTIAENS J., WOLF T.D., SORGELOOS P., BONTE D. & ADRIAENS D. (2017). Ontogenesis of opercular deformities in gilthead sea bream *Sparus aurata*: a histological description. *Journal of Fish Biology* 91: 1419–1434. https://doi.org/10.1111/jfb.13460

THUONG N.P., DIERICK M., DE WOLF T. & ADRIAENS D. (2018). A 3D quantitative method for analyzing bone mineral densities: a case study on skeletal deformities in the gilthead sea bream, *Sparus aurata* (Linnaeus, 1758). *Belgian Journal of Zoology* 148. https://doi.org/10.26496/bjz.2018.24

TOTLAND G.K., FJELLDAL P.G., KRYVI H., LØKKA G., WARGELIUS A., SAGSTAD A., HANSEN T. & GROTMOL S. (2011). Sustained swimming increases the mineral content and osteocyte density of salmon vertebral bone. *Journal of Anatomy* 219: 490–501. https://doi.org/10.1111/j.1469-7580.2011.01399.x

UTTING J.C., ROBINS S.P., BRANDAO-BURCH A., ORRISS I.R., BEHAR J. & ARNETT T.R. (2006). Hypoxia inhibits the growth, differentiation and bone-forming capacity of rat osteoblasts. *Experimental Cell Research* 312: 1693–1702. https://doi.org/10.1016/j.yexcr.2006.02.007

VALVERDE J.C., LÓPEZ F.J.M. & GARCÍA B.G. (2006). Oxygen consumption and ventilatory frequency responses to gradual hypoxia in common dentex (*Dentex dentex*): basis for suitable oxygen level estimations. *Aquaculture* 256: 542–551. https://doi.org/10.1016/j.aquaculture.2006.02.030

VERHAEGEN Y., ADRIAENS D., DE WOLF T., DHERT P. & SORGELOOS P. (2007). Deformities in larval gilthead sea bream (*Sparus aurata*): A qualitative and quantitative analysis using geometric morphometrics. *Aquaculture* 268: 156–168. https://doi.org/10.1016/j.aquaculture.2007.04.037

VLASSENBROECK J., DIERICK M., MASSCHAELE B., CNUDDE V., VAN HOOREBEKE L. & JACOBS P. (2007). Software tools for quantification of X-ray microtomography at the UGCT. *Nuclear Instruments and Methods in Physics Research Section A: Accelerators, Spectrometers, Detectors and Associated Equipment* 580: 442–445. https://doi.org/10.1016/j.nima.2007.05.073

WANG T., LEFEVRE S., VAN CONG N. & BAYLEY M. (2009). The effects of hypoxia on growth and digestion. *Fish Physiology* 27: 361–396. https://doi.org/10.1016/S1546-5098(08)00008-3

WINTERBOTTOM R. (1973). A descriptive synonymy of the striated muscles of the Teleostei. *Proceedings of the Academy of Natural Sciences of Philadelphia*: 225–317.

WITTEN P.E. & HALL B.K. (2015). Teleost skeletal plasticity: modulation, adaptation, and remodelling. *Copeia* 103: 727–739. https://doi.org/10.1643/CG-14-140

WITTEN P.E. & HUYSSEUNE A. (2009). A comparative view on mechanisms and functions of skeletal remodelling in teleost fish, with special emphasis on osteoclasts and their function. *Biological Reviews* 84: 315–346. https://doi.org/10.1111/j.1469-185X.2009.00077.x

WU Z., YOU F., WEN A., MA D. & ZHANG P. (2016). Physiological and morphological effects of severe hypoxia, hypoxia and hyperoxia in juvenile turbot (*Scophthalmus maximus* L.). *Aquaculture Research* 47: 219–227. https://doi.org/10.1111/are.12483

Manuscript received: 3 March 2023
Manuscript accepted: 12 June 2023
Published on: 20 July 2023
Branch editor: Isa Schön